# Structural Insights into the Dimeric Form of Bacillus subtilis RNase Y Using NMR and AlphaFold

Nelly Morellet, Pierre Hardouin, Nadine Assrir, Carine van Heijenoort, Béatrice Golinelli-Pimpaneau

▶ **To cite this version:**

Nelly Morellet, Pierre Hardouin, Nadine Assrir, Carine van Heijenoort, Béatrice Golinelli-Pimpaneau. Structural Insights into the Dimeric Form of Bacillus subtilis RNase Y Using NMR and AlphaFold. Biomolecules, 2022, 12 (12), pp.1798. 10.3390/biom12121798 . hal-04106119

**HAL Id: hal-04106119**
**https://hal.science/hal-04106119**

Submitted on 25 May 2023

**HAL** is a multi-disciplinary open access archive for the deposit and dissemination of scientific research documents, whether they are published or not. The documents may come from teaching and research institutions in France or abroad, or from public or private research centers.

L'archive ouverte pluridisciplinaire **HAL**, est destinée au dépôt et à la diffusion de documents scientifiques de niveau recherche, publiés ou non, émanant des établissements d'enseignement et de recherche français ou étrangers, des laboratoires publics ou privés.

biomolecules

MDPI

*Article*

# Structural Insights into the Dimeric Form of *Bacillus subtilis* RNase Y Using NMR and AlphaFold

**Nelly Morellet [1,*,†], Pierre Hardouin [2,†], Nadine Assrir [1], Carine van Heijenoort [1] and Béatrice Golinelli-Pimpaneau [2,*]**

[1] Institut de Chimie Des Substances Naturelles, Université Paris-Saclay, CNRS, UPR 2301, 91198 Gif-Sur-Yvette, France
[2] Laboratoire de Chimie des Processus Biologiques, UMR 8229 CNRS, Collège de France Université, 75231 Paris, France
* Correspondence: nelly.morellet@cnrs.fr (N.M.); beatrice.golinelli@college-de-france.fr (B.G.-P.); Tel.: +33-1-69-82-37-62 (N.M.); +33-1-44-27-12-52 (B.G.-P.); Fax: +33-1-69-82-37-84 (N.M.); +33-1-44-27-14-83 (B.G.-P.)
† These authors contributed equally to this work.

**Abstract:** RNase Y is a crucial component of genetic translation, acting as the key enzyme initiating mRNA decay in many Gram-positive bacteria. The N-terminal domain of *Bacillus subtilis* RNase Y (Nter-BsRNaseY) is thought to interact with various protein partners within a degradosome complex. Bioinformatics and biophysical analysis have previously shown that Nter-BsRNaseY, which is in equilibrium between a monomeric and a dimeric form, displays an elongated fold with a high content of α-helices. Using multidimensional heteronuclear NMR and AlphaFold models, here, we show that the Nter-BsRNaseY dimer is constituted of a long N-terminal parallel coiled-coil structure, linked by a turn to a C-terminal region composed of helices that display either a straight or bent conformation. The structural organization of the N-terminal domain is maintained within the AlphaFold model of the full-length RNase Y, with the turn allowing flexibility between the N- and C-terminal domains. The catalytic domain is globular, with two helices linking the KH and HD modules, followed by the C-terminal region. This latter region, with no function assigned up to now, is most likely involved in the dimerization of *B. subtilis* RNase Y together with the N-terminal coiled-coil structure.

**Keywords:** RNase Y; ribonuclease; NMR; AlphaFold; coiled-coil; structure; dimerization

check for updates

**Citation:** Morellet, N.; Hardouin, P.; Assrir, N.; van Heijenoort, C.; Golinelli-Pimpaneau, B. Structural Insights into the Dimeric Form of *Bacillus subtilis* RNase Y Using NMR and AlphaFold. *Biomolecules* **2022**, *12*, 1798. https://doi.org/10.3390/biom12121798

Academic Editor: Umesh Desai

Received: 23 September 2022
Accepted: 28 November 2022
Published: 1 December 2022

**Publisher's Note:** MDPI stays neutral with regard to jurisdictional claims in published maps and institutional affiliations.

**Copyright:** © 2022 by the authors. Licensee MDPI, Basel, Switzerland. This article is an open access article distributed under the terms and conditions of the Creative Commons Attribution (CC BY) license (https://creativecommons.org/licenses/by/4.0/).

## 1. Introduction

In bacteria, gene expression in response to different environmental conditions is controlled by the fluctuation of messenger RNA (mRNA) transcript abundance [1–3]. The rapid mRNA turnover rate in bacteria (average half-life of several minutes) relies on the synthesis and degradation rates of each mRNA. RNases, responsible for RNA degradation, can be either very specific for their RNA substrate or be involved in bulk RNA turnover. The major RNases involved in bulk RNA turnover generally form multi-protein complexes for efficient and regulated degradation, which are called RNA degradosomes [4]. While most RNA synthesis machinery is similar in Gram-negative and Gram-positive bacteria, the machinery for bulk RNA degradation is quite different. In *Escherichia coli*, the well-studied hydrolytic endoribonuclease RNase E plays a major role in mRNA degradation and RNA processing [5], whereas RNase Y is one of the key enzymes directing RNA metabolism in *Bacillus subtilis* [6] as well as in other low-GC Gram positive species [7], including many pathogens [8–10]. Moreover, RNase Y was shown to be necessary for the full virulence of several Gram-positive bacterial pathogens [8,11]. Studying the function and structure of RNase Y is not only crucial to understand RNA metabolism in the many eubacteria that, unlike *E. coli*, do not rely on RNase E-based strategies of RNA degradation/maturation, but also to consider whether RNase Y could be targeted for the development of new

antimicrobial agents against Gram-positive bacteria in the future, since RNase Y orthologs do not exist in eukaryotic cells.

While RNase Y and RNase E share many functions [12], they display only low sequence similarity (Figure 1). *E. coli* RNase E (1061 amino acids; 118 kDa) is composed of two major domains: the N-terminal domain that bears the endoribonuclease activity [13–15] and the C-terminal scaffolding domain that organizes the RNA degradosome [4,16–18] (Figure 1A).

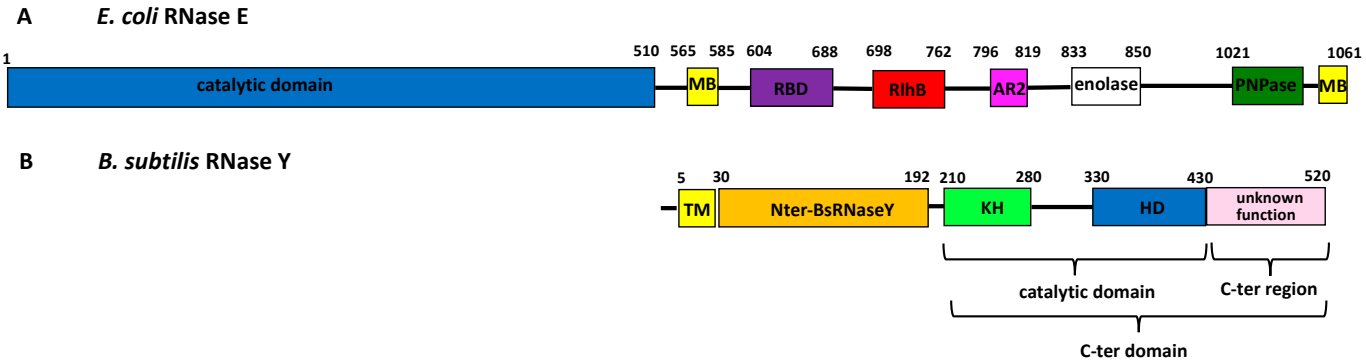


**Figure 1.** Comparison of the domain organization of *E. coli* RNase E and *B. subtilis* RNase Y. (**A**) Schematic representation of *E. coli* RNase E showing the interactions with proteins from the degradosome machinery (adapted from [19]). RBD and AR2 are arginine-rich RNA-binding domains flanking the RhlB (helicase) binding site and MB are membrane-binding domains. (**B**) Schematic representation of *B. subtilis* RNase Y. The catalytic domain contains KH and HD motifs. The KH homology module is a widespread RNA-binding motif, whereas the HD motif is characteristic of a superfamily of metal-dependent phosphohydrolases. TM is the transmembrane sequence. In this figure, the delimitation of the domains is based on the amino acids sequence.

This latter domain is intrinsically unstructured and unlikely to be extensively folded within the degradosome complex, except for a few microdomains that are conserved among RNase E orthologs [20,21]. The C-terminal microdomain, called the membrane targeting sequence, forms an amphipathic helix that interacts with the membrane [22]. Other conserved microdomains, ranging from 20 to 70 residues in size, are binding sites for RNA substrates and other protein components of the degradosome [20], including enolase [23,24] and PNPase [25]. *B. subtilis* RNase Y (529 amino acids; 58.9 kDa) is much shorter than *E. coli* RNase E and its catalytic domain is located at the C-terminus [12]. A transmembrane (TM) region, anchoring the protein to the membrane, is followed by the N-terminal domain and the C-terminal domain, itself composed of the catalytic domain with KH [26] and HD modules [27] and a C-terminal region of unknown function (Figure 1B).

Interestingly, RNase E was recently shown to be able to replace RNase Y in *B. subtilis* in vivo [28]. Efficient complementation of the *B. subtilis* Δ*rny* strain required RNase E to be localized to the inner membrane, while truncation of the C-terminal domain corresponding to the degradosome scaffold had only a minor effect.

The three-dimensional (3D) structure of RNase Y remains unknown. *B. subtilis* RNase Y lacking the TM region has previously been purified and analyzed by sedimentation velocity analytical ultracentrifugation, which showed that it is divided into an aggregated form and a mixture of dimers and tetramers [29]. The analysis of the interaction of the isolated domains (TM, N-terminal, and C-terminal) with each other, using a bacterial two-hybrid system [30], revealed that only the TM and the N-terminal domains showed self-interactions [12], suggesting that they were major contributors to the oligomerization of RNase Y. Although some bioinformatic programs (PONDR-FIT and metaPrDOS) predicted that the N-terminal domain is intrinsically disordered, others, such as COILS [12] or Lupas' algorithm [31] (Figure S1A,B) indicated that it is organized mainly as α-helices, adopting a flexible coiled-coil-like structure. In Lupas' coiled-coil prediction [31], the probability of the N-terminal domain to form a coiled-coil structure was higher than 80% for residues

30–103, whatever the parameters used, and higher than 50% or 90% for residues 104–153. In addition, the protein fold recognition servers PSIPRED, PHYRE2, and the consensus secondary structure prediction server NPS@ predicted that the N-terminal domain adopts a helix-type secondary structure over almost the entire sequence (Figure S1C–E).

We recently produced the N-terminal domain as a stand-alone protein called Nter-BsRNaseY and characterized its secondary structure by circular dichroism (CD) spectroscopy, size exclusion chromatography coupled with multi-angle light scattering (SEC-MALS), and size exclusion chromatography coupled with small-angle X-ray scattering (SEC-SAXS) [32]. Monitoring the weight-averaged molar mass as a function of protein concentration showed that the dimeric form of Nter-BsRNaseY is in equilibrium with a monomeric form, with a dissociation constant $K_d$ of 1.3 µM. Nter-BsRNaseY was bound as a monomer when complexed with Fab (fragment antigen binding), which suggested that dissociation of the dimer could occur upon binding a protein partner [32]. Moreover, the dimer was shown to display an elongated form and a high content of α-helices [32].

*B. subtilis* RNase Y has been proposed to participate, together with polynucleotide phosphorylase PNPase, helicase CshA, and the glycolytic enzymes 6-phosphofructokinase and enolase in a multiprotein complex [33–38], similar to the RNase E-based degradosome in *E. coli* (Figure 1). Whereas PNPase is an RNA 3′ exoribonuclease and helicases are known to play important roles in remodeling RNA molecules, the function of the glycolytic enzymes within the complex is more elusive. Enolase is one intracellular/surface moonlighting protein present in many species, including eukaryotes and prokaryotes [39]. Inside the cell, it catalyzes the conversion of 2-phosphoglycerate to phosphoenolpyruvate in glycolysis. Yet, in some species, enolase is displayed on the cell surface, which allows it to play a role in bacterium–host interactions [40] by binding to host proteins such as plasminogen [41] and fibronectin [42]. It has been suggested that the N-terminal domain of RNase Y is the key element for assembling a degradosome complex in *B. subtilis* [33], similar to the C-terminal domain of RNase E in *E. coli* [41]. Therefore, as a first step to understand the functional importance of the N-terminal domain, here, we studied the structure of Nter-BsRNaseY using multidimensional heteronuclear NMR and the structure prediction algorithm AlphaFold [43]. Moreover, we also discuss the model of the full-length protein predicted by AlphaFold.

## 2. Materials and Methods

### *2.1. Prediction of the Secondary Structure of Nter-BsRNaseY*

The secondary structure of Nter-BsRNaseY was analyzed with the protein fold recognition servers PHYRE2 (http://www.sbg.bio.ic.ac.uk/phyre2/html/page.cgi?id=index, accessed on 22 September 2022) [44], PSIPRED (https://bio.tools/psipred, accessed on 22 September 2022) [45], and the consensus secondary structure prediction server NPS@ (https://npsa-prabi.ibcp.fr/cgi-bin/npsa_automat.pl?page=/NPSA/npsa_seccons.html, accessed on 22 September 2022) [46]. The coiled-coil structure was predicted using (https://npsa-prabi.ibcp.fr/cgi-bin/npsa_automat.pl?page=/NPSA/npsa_lupas.html, accessed on 22 September 2022) either with or without a weight of 2.5 for positions 'a' and 'd' of the heptad repeat for windows of 14, 21, and 28 residues, knowing that the use of a weight for certain residues increases the prediction for a dimerization interface centered on these residues. The helical wheel plots were drawn with DrawCoil 1.0 [47].

### *2.2. Three-Dimensional Structure Prediction of Nter-BsRNaseY and Full-Length RNase Y Using AlphaFold*

The AlphaFold models of Nter-BsRNaseY and full-length RNase Y were calculated for the untagged proteins with the Google Colab platform and AlphaFold2_advanced option https://colab.research.google.com/github/sokrypton/ColabFold/blob/main/beta/AlphaFold2_advanced.ipynb#scrollTo=ITcPnLkLuDDE, accessed on 22 September 2022 [43,48] that does not use templates (homologous structures) and refined using the Amber-relax option to enhance the accuracy of the side chains' geometry. The default

mode of sampling options was used: num_models = 5, ptm option, num_ensemble = 1, max_cycles = 3, tol = 0, num_samples = 1. The models were ranked according to their predicted local-distance difference test (pLDDT) confidence values (between 0 and 100, from low to high confidence). In the AlphaFold model file, the B-factor column for each residue is populated with its pLDDT value. For dimer prediction, a 1:1 value was input as the homo-oligomer assembly option. The structure figures were drawn with PYMOL [49].

### *2.3. Production of Nter-BsRNaseY*

Methods for cloning the coding sequence corresponding to Nter-BsRNaseY (amino acids V24 to N192 of *B. subtilis* RNase Y), appended with a C-terminal hexahistidine tag, were described previously, as well as the production and purification of the protein [32]. Protein elution was followed by the optical density at 230 nm because of the absence of aromatic residues in the Nter-BsRNaseY sequence.

### *2.4. Culture and Purification of $^{15}$N-Labeled and $^{13}$C-$^{15}$N-$^{2}$D-Labeled Nter-BsRNaseY*

For preparation of $^{15}$N-labeled Nter-BsRNaseY, cell growth was performed in 1L M9 minimal medium containing $^{15}$N-labeled $NH_4Cl$, supplemented with 2 mM $Mg_2SO_4$, 4 g/L glucose, 10 µM $CaCl_2$, 1 mg/L biotin, 5 mg/L thiamine, 50 µg/mL ampicillin, and 30 µg/mL chloramphenicol. For preparation of $^{13}$C-$^{15}$N-$^{2}$D-labeled Nter-BsRNaseY, cell growth was performed in 1L of M9 minimal medium containing $D_2O$ and $^{15}$N-labeled $NH_4Cl$, supplemented with 2 mM $MgSO_4$, 3 g/L [$^{13}$C]-glucose, 10 µM $CaCl_2$, 1 mg/L biotin, 5 mg/L thiamine, 50 µg/mL ampicillin, and 30 µg/mL chloramphenicol. The proteins were purified by Ni-NTA affinity and SEC, as described [32], then by SEC on a Superdex Increase 200 10/300 GL increase column in 20 mM HEPES pH 7.5, 500 mM NaCl, 10% glycerol for $^{15}$N-labeled Nter-BsRNaseY, or 40 mM MES pH 6.8, 200 mM NaCl for $^{13}$C-$^{15}$N-$^{2}$D-labeled Nter-BsRNaseY (Figure S2A). Finally, $^{15}$N-labeled and $^{13}$C-$^{15}$N-$^{2}$D-labeled Nter-BsRNaseY were concentrated to 10 mg/mL (240 µM) or 40 mg/mL, respectively, using Amicon concentrators (30 kDa cutoff, Milllipore), then aliquoted, frozen in liquid nitrogen, and stored at −80 °C.

### *2.5. Circular Dichroism of Nter-BsRNaseY*

The far-UV CD spectrum (195−260 nm) of Nter-BsRNaseY was recorded at various temperatures (293, 298, 300, 303, 313, and 318K) on a Chirascan-plus CD spectrometer (Applied Phtophysics, Surrey, UK) (Figure S2B). Spectra of Nter-BsRNaseY (450 µM) were acquired in quartz cuvettes of 0.01 mm optical path length in 40 mM MES pH 6.8, 200 mM NaCl. A resolution of 1 nm, bandwidth of 1 mm, and time per points of 1s were applied. All spectra, resulting from an average of ten accumulations, were corrected from buffer contribution.

### *2.6. NMR Resonance Assignments for RNase Y Backbone*

NMR samples of $^{13}$C-$^{15}$N-$^{2}$D-labeled Nter-BsRNAseY (970 µM) were prepared in 40 mM MES buffer pH 6.8, 200 mM NaCl, 5% $D_2O$ for the reference condition. A series of 2D $^{1}$H-$^{15}$N BEST-Transverse relaxation optimized spectroscopy (TROSY) correlation spectra were recorded at 278K, 288K, 293K, 298K, 303K, 308K, 313K, and 318K, and a series of 3D BEST-TROSY (HNCA, HNCOCA, HNCACB, HNCOCACB, HNCO, and HNCACO) correlation spectra were collected at 300, 303, and 313K on a Bruker AVANCE III HD 950 MHz equipped with a TCI cryoprobe. A series of BEST-TROSY correlation spectra were also recorded at 303K at various concentrations of Nter-BsRNAseY (50, 98, 185, and 332 µM). A 3D $^{1}$H-$^{15}$N nuclear Overhauser effect spectroscopy (NOESY)-heteronuclear single quantum correlation (HSQC) spectrum, with mixing times of 200 ms, was also collected to help peaks assignment at 303K. Data processing and analysis were performed using the Topspin® 4.0 and CcpNmr version-2 software [50]. To record the spectrum of the completely denatured protein, the buffer was supplemented by 6 M urea. The $^{15}$N $R_1$ and $R_2$ relaxation rates and {$^{1}$H}-$^{15}$N heteronuclear nuclear Overhauser effects (NOEs) were

measured at 303K. The $^{15}N$ $R_1$ and $R_2$ relaxation experiments were based on the refocused $^{1}H$-$^{15}N$ HSQC relaxation experiments and recorded in an interleaved pseudo-3D method with an inter-scan delay of 4 s. For the determination of $R_1$ relaxation rate constants, 11 total data sets were collected at relaxation delay times of 10, 50, 100, 200, 400, 500, 600, 800, 1000, 1500, and 2000 ms. For the determination of $R_2$ rate constants, 12 data sets were collected at delay times of 17, 34, 51, 68, 84.8, 102, 136, 170, 204, 237, 271, and 305 ms. $R_1$ and $R_2$ spectra were recorded as 144 × 2024 complex data points. For the backbone $\{^{1}H\}$-$^{15}N$ heteronuclear NOEs, two different spectra were recorded as 256 × 2048 complex data points in an interleaved manner with and without a 4 s proton saturation pulse. The $R_1$ and $R_2$ rates, heteronuclear NOE values, and their associated errors were determined from the peak intensities using the CcpNmr version-2 software [50].

The amide proton chemical shift temperature coefficients ($\Delta\delta HN/\Delta T$ (ppb/K)) were calculated using the Shift-T web server (http://biophysical.science/shiftt, accessed on 22 September 2022) [51].

## 3. Results

### *3.1. Several Regions of Nter-BsRNaseY Have a High Propensity to Form α-Helices*

To study the structure of Nter-BsRNaseY by NMR, the protein was expressed in *E. coli* and labeled with $^{15}N$ or $^{15}N$, $^{13}C$, and $^{2}D$. Its $^{1}H$-$^{15}N$ BEST-TROSY spectrum was first recorded at 300K and a concentration of 970 µM, under which conditions Nter-BsRNaseY is a dimer [32]. The TROSY spectrum, which provides correlations between nitrogen atoms and amide protons, shows a narrow chemical shift dispersion in the $^{1}H$ dimension (gathered in the 7.9–8.5 ppm region) that is characteristic of rather disordered or α-helices-forming residues (Figure 2A,B).

To confirm that the protein contains ordered structural elements, the $^{1}H$-$^{15}N$ heteronuclear multiple quantum coherence (HMQC) spectrum was compared to that of a denatured sample (Figure S3). The addition of 6 M urea, a widely used protein denaturing agent [52], resulted in substantial sharpening of the chemical shifts for most signals, as well as in several significant chemical shift variations. These changes indicate the disappearance of structured elements, probably resulting from a change of inter-molecular interactions.

To obtain more information about the secondary structure of the different regions of Nter-BsRNaseY at the residue level, we assigned the amide $^{1}H$, $^{15}N$ and $^{13}C$ resonances using the standard triple experiments at 300, 303, and 313K (Figure S4). The CD spectrum of BsRNAseY was also recorded at these temperatures, as well as at 298 and 318K, to monitor the signal at 220 nm and thus the variation in the α-helices content with temperature (Figure S2B). We assigned the resonances for 157 out of 176 (89%) of the Nter-BsRNaseY backbone atoms. Assignment is missing for the three N-terminal amino acids (M23-R25) and for residues H67-K68, R81, H102, D116-S118, R122-H125, M139-Q140, M161-R162, and H169. We note that the five histidine residues of Nter-BsRNaseY (H67, H102, H117, H125, and H169) are localized within these segments. The Nter-BsRNaseY $^{13}CO$, $^{13}C_{\alpha}$, $^{13}C_{\beta}$, $^{1}H_{N}$, and $^{15}N$ chemical shifts were then used as input for the TALOS-N software [53] to predict the protein backbone torsion angles along the sequence. The TALOS-N results reveal that several regions of the protein (residues 39–61, 73–88, 122–157, and 171–191) have the highest propensity to form α-helices at 300K (Figure 3A and Table S1).

In regular turns and α-helical polypeptide chains, sequential amide protons close in space ($HN_i$-$HN_{i+1}$) yield to cross-peaks of high intensity in the NOESY spectra, while protons farther away ($HN_i$-$HN_{i+2}$) give peaks of lower intensity. We analyzed the $^{1}H$-$^{15}N$ (HSQC)-NOESY 3D spectrum to delineate the helical motifs (Figure S5). Despite a lot of overlapped peaks, we were able to find NOEs corresponding to several amide protons HN32-HN34, HN55-HN57, HN109-HN112, HN136-HN138, and HN142-HN144 (Figure S5A). HN55-HN57 is located in the first helix predicted by TALOS-N, HN109-HN112 is located in the second helix, whereas HN136-HN138 and HN142-HN144 are located in the third helix (Table S1).

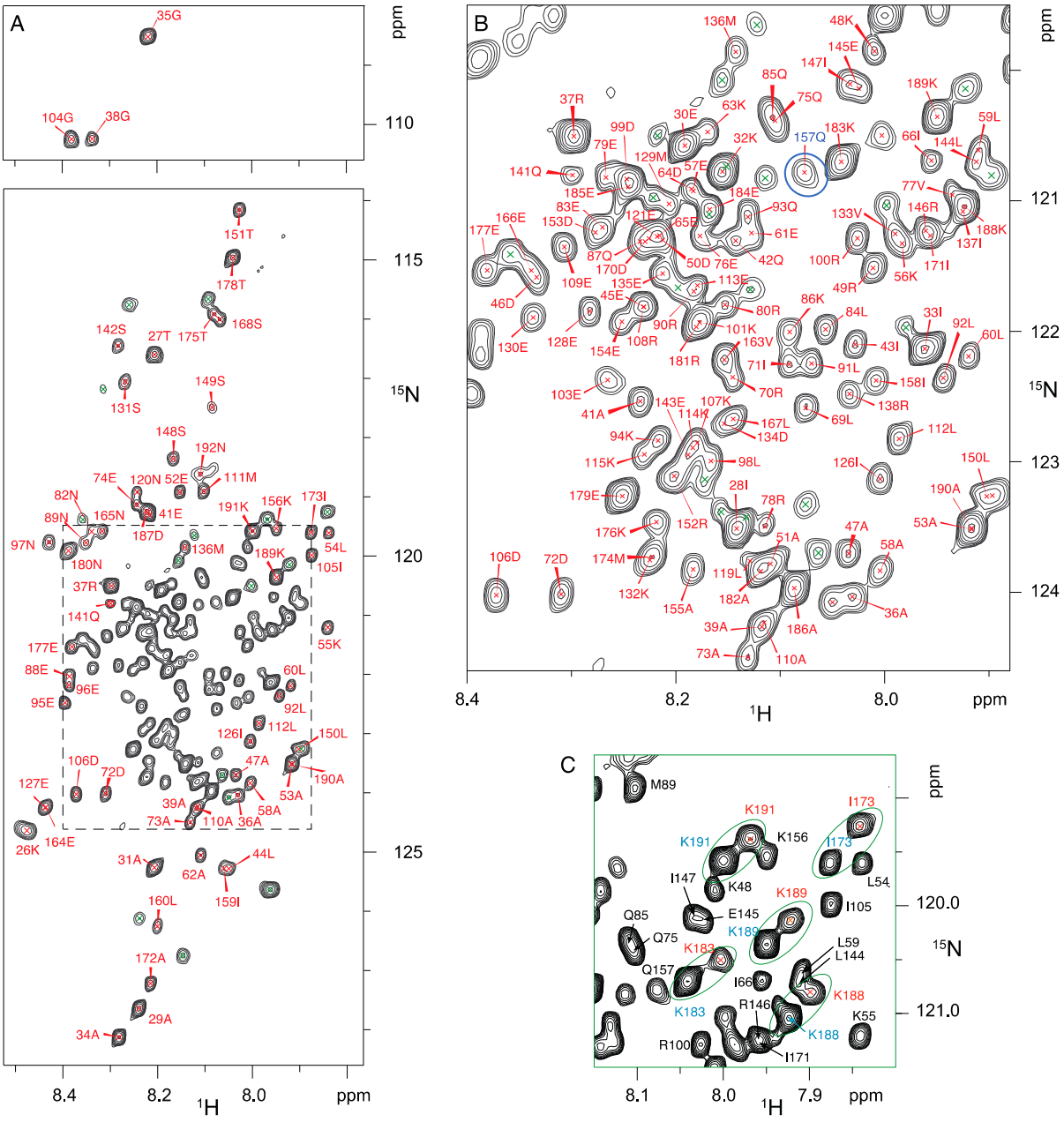


**Figure 2.** $^{1}$H-$^{15}$N BEST-TROSY spectrum of 970 µM $^{15}$N-$^{13}$C-$^{2}$D-labeled Nter-BsRNaseY. The spectrum was recorded at 950 MHz, in 40 mM MES buffer pH 6.8, 200 mM NaCl, 300K. (**A**) Overall spectrum and (**B**) enlarged view of framed region. Several peaks, such as Q157 (circled in blue), display a weak intensity. (**C**) Region of the $^{1}$H-$^{15}$N BEST-TROSY spectrum of Nter-BsRNaseY showing several duplicated peaks, marked in blue (higher intensity peaks) and in red (lower intensity peaks). Pairs of split peaks are circled in green. The peaks that are not duplicated are marked in black.

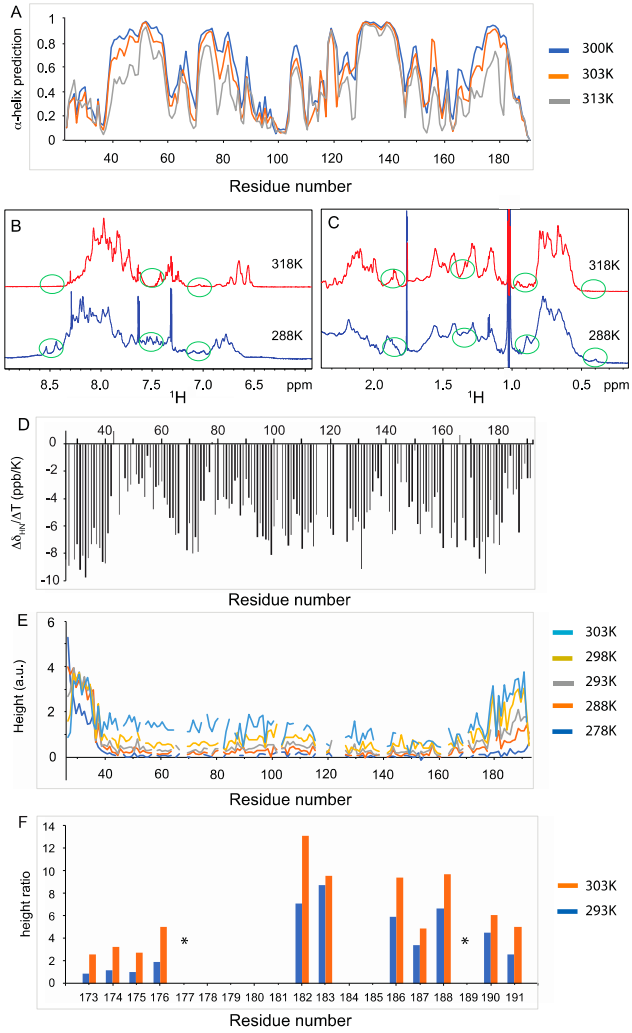


**Figure 3.** Flexibility and helix propensity of Nter-BsRNaseY amino acids, as deduced from the $^{1}$H-$^{15}$N-$^{13}$C NMR data. (**A**) Prediction of α-helices propensity by TALOS, derived from the backbone NMR chemical shifts at 300K (in blue), 303K (in orange), and 313K (in grey). Comparison of the amide and aromatic (**B**) and aliphatic protons (**C**) in the 1D NMR spectra recorded at 288K (in blue) and 318K (in red). The green circles highlight the highest differences observed in the chemical shifts at the two temperatures. (**D**) Temperature coefficients (ΔδHN/ΔT (ppb/K)). (**E**) $^{1}$H-$^{15}$N TROSY peak heights (arbitrary units) at 278, 288, 293, 298, and 303K. The peak heights for residues 170 to 192 are the sum of the corresponding duplicated peaks in the $^{1}$H-$^{15}$N TROSY spectra. (**F**) Comparison of the peak height ratio in the $^{1}$H-$^{15}$N BEST-TROSY spectra of pairs of duplicated peaks for several residues located in the 173–191 segment at 293K (in blue) and 303K (in orange). The peaks in Figure S7A,B were used to calculate the peak height ratios. * indicates that the peak height ratio could not be measured because the duplicated peaks of E177 and K189 are superimposed onto other peaks.

The 133–149 helix appears to be the most stable helix since it is present at both 300 and 313K (Figure 3A), with the same predictions for all amino acids. Interestingly, we observed a significant increase in the percentage of α-helices as the temperature decreases (36% at 313K but 65% at 300K), as predicted by TALOS-N (Table S1). This increased folding of the protein with a decrease in temperature, with a break in the α-helix content between 303 and 300K, was also observed on the CD (Figure S2B) and $^{1}$H spectra (Figure S6). Indeed, a decrease from 318K to 288K, leads to a deshielding (shifting to higher ppms) of some amide protons (between 8.4 and 8.6 ppm), a higher chemical shift dispersion of peaks between 6.9 and 7.7 ppm (Figures 3B and S6A), as well as a shielding of several methyl groups around 0.4 ppm (Figures 3C and S6B). Numerous amide proton temperature coefficients

($\Delta\delta HN/\Delta T$) were higher than −5 ppb/K (Figure 3D), indicating a high probability for these amide protons to be hydrogen bonded [54]. Interestingly, these residues belong mainly to the regions of the protein described above that have a high propensity to form α-helices.

To obtain further insights into the flexibility of Nter-BsRNaseY, we analyzed the changes in the $^{1}H$-$^{15}N$ TROSY cross-peak intensities as a function of temperature (Figure 3E). In such spectra, the intensity of the peaks varies with the mobility of the corresponding residues, with the higher flexible regions showing higher peak intensities. We observed that the N-terminal residues (20 to 35) and the C-terminal extremity (residues 176–192) of Nter-BsRNaseY belong to the most flexible regions of the protein. For the N-terminal region, the peak intensities showed little variation with temperature, indicating that flexibility was inherent to this region and not dependent on temperature. In contrast, whereas the C-terminal region was only slightly more flexible than the rest of the protein at low temperature (278K), its flexibility increased much faster with temperature than the rest of the protein (Figure 3E).

### *3.2. Two Main Conformations of the C-Terminal Extremity of Nter-BsRNaseY*

The analysis of the $^{1}H$-$^{15}N$ BEST-TROSY spectra of Nter-BsRNaseY at various temperatures (Figure S7) allowed us to assign two sets of amide peaks corresponding to two conformations for several residues belonging to the C-terminal extremity (residues 171–191 (Figures 2C and S7A,B). Yet, it was not possible to assign duplicated peaks for residues N180, R181, E184, and E185 because their intensity was too low to be detected in the 3D spectrum (Figure S7C).

The relative intensity of the duplicated cross-peaks decreased with temperature, indicating a change in conformers ratio (Figure S7A). Between 293 and 308K, the duplicated cross-peaks were clearly visible, suggesting that residues 171–191 switch between two conformations at a slow rate on the NMR time scale (~millisecond range). Above 308K, only one cross-peak per residue was observed, indicating the presence of a single conformer. Interestingly, we noticed that the intensity ratio between the pairs of peaks of residues 173–176 is lower than that of residues 182–191 (Figure 3F). This indicates that the C-terminal residues (182–191) are more sensitive to temperature than residues 173–176.

In addition, we recorded a series of BEST-TROSY spectra at various concentrations of Nter-BsRNAseY (50–332 μM) and 303K in order to evaluate the influence of protein concentration on the duplicated cross peaks in the $^{1}H$-$^{15}N$ BEST-TROSY spectra (Figure S8). At all these concentrations, Nter-BsRNaseY was shown to be a dimer [32]. The comparison of the spectra of Nter-BsRNaseY at low and high concentrations (50 μM and 970 μM, respectively) showed no significant chemical shift variations. However, peaks duplication was not observed at low protein concentration for the C-terminal residues (residues 171–191) (Figure S8). This suggests a concentration-dependent change in the equilibrium between two species that display different conformations of the C-terminal residues.

### *3.3. High Flexibility of the N- and C-Terminal Residues*

In addition, we also observed variations in the peaks in the $^{1}H$-$^{15}N$ BEST-TROSY spectrum, with some of them showing a significantly weaker intensity than the others (Figure 2B). To determine if this results from a conformational change of the protein, we studied the dynamics of the Nter-BsRNaseY backbone using NMR $^{15}N$ relaxation, which is a powerful tool to characterize dynamic processes of proteins in solution over a wide range of time scales [55]. Indeed, on one hand, fast motions (picosecond to nanosecond scale) can be characterized by heteronuclear $^{15}N$ longitudinal relaxation rate ($R_1$), transverse relaxation rate ($R_2$), and $^{15}N$-{$^{1}H$} heteronuclear NOE (hetNOE) of amide group resonances; on the other hand, chemical exchange mechanisms are generally involved in movements on the microsecond-millisecond scale and contribute to the $R_2$ transverse relaxation rate. Thus, heteronuclear NOEs are very sensitive to local mobility, with large NOE values indicating restricted motion.

NMR $^{15}$N relaxation measurements at 950 MHz $^{1}$H and 303K of Nter-BsRNaseY show that the $R_1$ and hetNOE relaxation rates are relatively homogeneous over the regions encompassing residues 40 to 115 and 170 to 191 (Figure 4A,C).

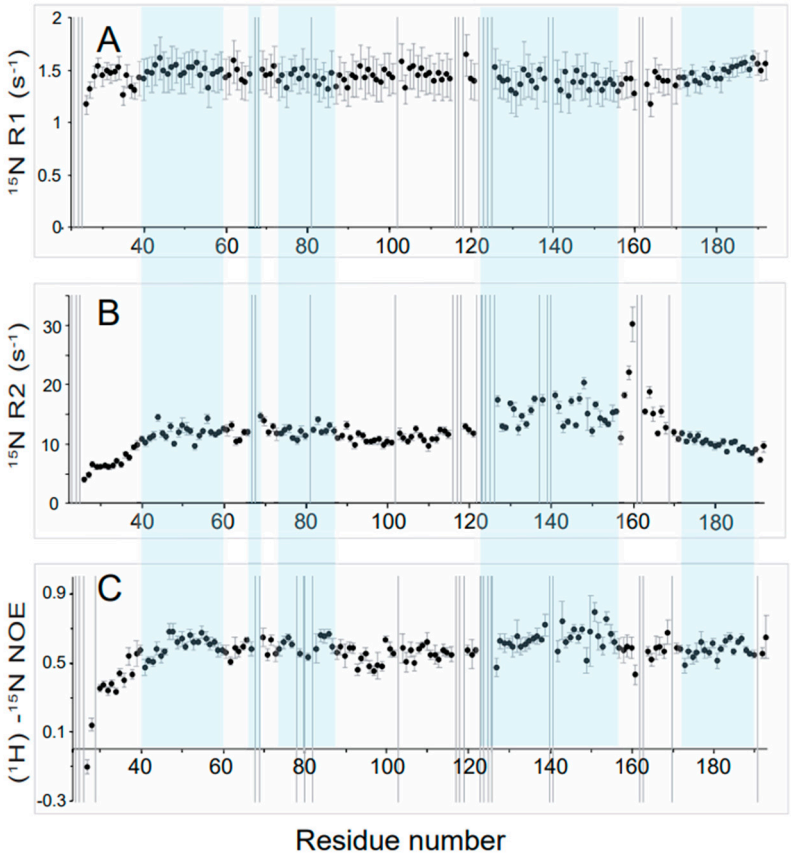


**Figure 4.** Relaxation rates and backbone dynamics of Nter-BsRNaseY. Plots of the $^{15}$N longitudinal relaxation rate $R_1$ (**A**), $^{15}$N transverse relaxation $R_2$ (**B**), heteronuclear {$^{1}$H}-$^{15}$N NOE, and (**C**) parameters obtained at 950 MHz $^{1}$H and 303K as a function of residue number. The unassigned residues of Nter-BsRNaseY are represented by vertical grey lines. The helices predicted by TALOS-N are highlighted in light blue.

Higher $R_2$ and hetNOEs values than average were observed for residues belonging to the 127–155 segment (Figure 4B,C), suggesting reduced mobility. Accordingly, up to 313K, this region was shown to have a high propensity to adopt an α-helix fold (Figure 3A). On the contrary, the N-terminal extremity (residues 24–39) showed lower $R_2$ and hetNOE values than the rest of the polypeptide chain, indicating a high flexibility of this segment. Moreover, for the segment 158–170, low hetNOE values were observed (Figure 4C), indicating an increase in mobility, as well as high $^{15}$N $R_2$ values (Figure 4B), likely resulting from a contribution to µs-ms conformational or chemical exchange. These observations are consistent with the α-helix predictions (Figure 3A), which show that this segment has a low propensity to form an α-helix.

### *3.4. AlphaFold Models of Nter-BsRNaseY*

To calculate 3D models of Nter-BsRNaseY, we used the recently released AlphaFold algorithm [43], which has revolutionized structural biology by its highly accurate predictions of protein structures (Figure 5).

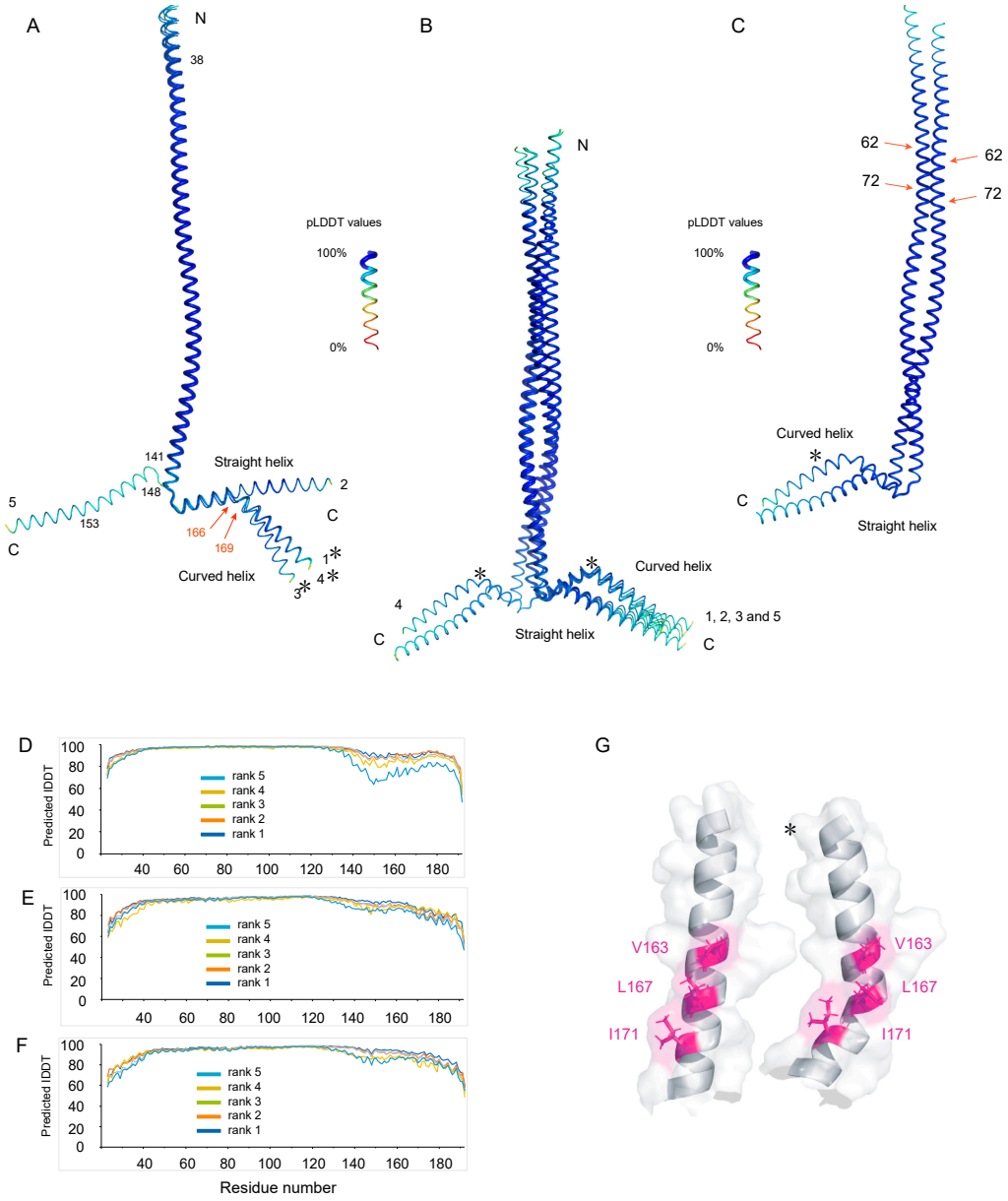


**Figure 5.** The five best 3D models of Nter-BsRNaseY generated by AlphaFold. The five models, numbered from 1 (best) to 5 (worst), were superimposed on the backbone of residues 33–138 that were shown to possess the best pLDDT values. (**A**,**B**): Superimposition of the AlphaFold models for the monomer (**A**) and dimer (**B**). (**C**) The best AlphaFold model of the dimer. The red arrows highlight the break in the supercoil. (**D**–**F**) pLDDT values for the AlphaFold models of the monomer (**D**) and the dimer: (**E**) first monomer and (**F**) second monomer. The residues were colored according to their pLDDT values, from red (0%) to blue (100%). (**G**) Hydrophobic interactions involving V163, L167, and I171, leading to the formation of a kink in the helical C-terminal extremity of the dimer helix. The curved helix is indicated by an asterisk.

AlphaFold was used to predict the 3D structure of both the monomer (Figure 5A) and the dimer (Figure 5B,C) because previous studies indicated that, at the concentration of Nter-BsRNaseY used for the NMR studies, Nter-BsRNaseY is in the dimeric form [32]. For both the monomer and dimer models, the AlphaFold prediction is highly reliable for residues 38 to 169, with predicted pLDDT values over 90 (Figure 5D–F), which means that, in addition to a good backbone prediction, the side chains are also correctly oriented. Nevertheless, the pLDDT values decreased gradually after residue 170—but still remained

above 80 until residue 188—for the best model of the monomer (Figure 5D) and the dimer (Figure 5E,F), indicating that the position of the C-terminal residues is less well predicted.

The monomer is constituted of a long α-helix (residues 23 to 149), followed by a turn (residues 150 to 151) and a C-terminal extremity (residues 152–192), which forms either a long straight helix or a curved helix with a kink around residues 166 to 169 (Figure 5A). Interestingly, in all dimer models, the interaction between the two monomers involves a long parallel coiled-coil structure containing two long α-helices (residues 23 to 149) (Figure 5B,C). No antiparallel coiled-coil structure was found in the best predictions for the Nter-BsRNaseY dimer by AlphaFold. In addition, the two long α-helices wrap around each other to form a left-handed supercoiled structure, but with a break in the supercoil around residues 62–72 (Figure 5C). The C-terminal extremity of the dimer is formed by a pair of helices, one straight helix from one monomer and one curved helix from the second monomer.

In a perfect coiled-coil structure, two α-helices pack against each other, with the amino acid side chains adopting a well-established architecture that is called a knob-into-hole (KIH) packing [56,57]. The typical coiled-coil sequence consists of a series of adjacent heptad repeats $(a\text{-}b\text{-}c\text{-}d\text{-}e\text{-}f\text{-}g)_n$, in which the residues at position 'a' are either apolar or charged (R, K, E and D) and the residues at position 'd' are usually hydrophobic (V, L, I). The long α-helix of the N-terminal part (residues 30–149) of Nter-BsRNaseY satisfies the conditions for forming a coiled-coil structure in a parallel orientation, involving extensive ionic and hydrophobic interactions, as illustrated by the helical wheel plots (Figure S9).

Hydrophobic side chains are present at the 'a' and 'd' positions of the 30–71 segment (Figure S9A), leading mainly to hydrophobic interactions between the two chains (Figure S10A,B), whereas hydrophobic side chains are present only at the 'd' positions of the 74–122 and 109–150 segments (Figure S9B,C), leading to both hydrophobic and electrostatic interactions (Figures S9B,C and S10C,D). In addition electrostatic interactions are observed between residues located at the 'e' and 'g,' positions (Figure S9A–C), 'd' and 'e' positions (Figure S9D), or 'a' and 'g' positions (Figure S9B,C). The charges of the residues located inside the helix, at positions 'a', 'd', 'e', and 'g' of the heptad repeat are of opposite sign, forming ionic interactions that stabilize the structure (yellow circles in Figure S10).

However, the N-terminal region (residues 30–71) does not adopt a canonical coiled-coil structure (Figure 5C), with many alanine residues being present at the 'a' position (instead of R, K, E and D) or 'd' position (instead of V, L, I), together with leucine and isoleucine (Figures S9A and S10A). The break in the supercoil noticed around residues 62–72 could result from the differences in the dimerization interfaces of the segments containing residues 30–71 (Figures S9A,B and S10A,B) on one hand and those containing residues 74–122 (Figures S9B and S10B,C) on the other hand.

Finally, the intermolecular interactions between the helical C-terminal extremities (residues 152–192) of each monomer involve hydrophobic and electrostatic interactions, but do not have the characteristics of a coiled-coil structure (Figures S9D and S10E,F). The kink in one helix (Figure 5B,C) is maintained through hydrophobic interactions between the two chains involving residues I158, I159, L160, V163, L167, I171, and M174 from each monomer (Figures 5G and S10E). Therefore, the different conformations of the two C-terminal extremities of the Nter-BsRNaseY dimer come from a different structural environment of residues 158–192 in the two chains.

### *3.5. AlphaFold Model of the Full-Length B. subtilis RNase Y*

Finally, we also used AlphaFold to model the structure of the monomer and dimer of full-length *B. subtilis* RNase Y (Figures 6 and S11) and fine-tune the boundaries of the C-terminal domain (Figure 1B) based on structural elements.

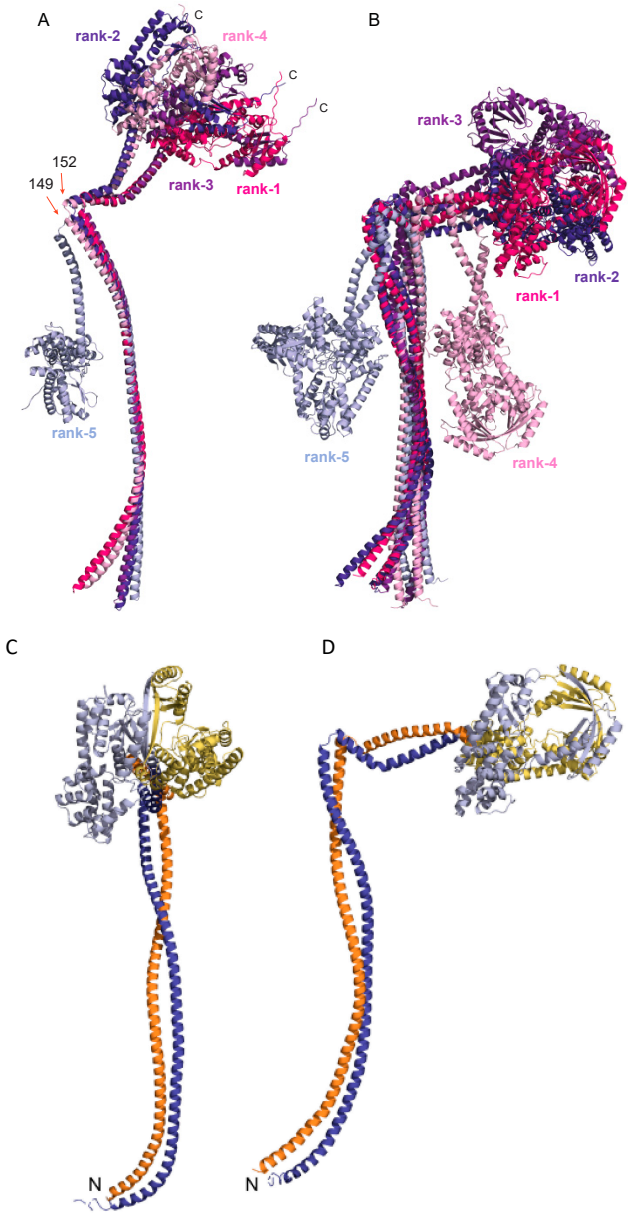


**Figure 6.** AlphaFold models of the full-length *B. subtilis* RNase Y. (**A**) The five best 3D models of the monomer. (**B**) The five best 3D models of the dimer. The models are numbered from 1 (the best) to 5 (the worst). The residues at the edges of the turn are highlighted as orange arrows. (**C**,**D**): Two different views showing the relative orientation of the two chains in the dimer of the best AlphaFold model for the full-length *B. subtilis* RNase Y. One chain is colored orange and yellow and the other is colored dark blue and light blue, for the N- and C-terminal domains, respectively.

As for Nter-BsRNaseY, in the monomer of *B. subtilis* RNase Y, the N-terminal domain is formed by a long α-helix composed of residues 23–147, followed by a turn involving residues 150–151 and a region, composed of residues 155–202, that adopted either a long straight helix or a curved helix with a kink around residues 167–171 (Figure 6A). Hence, some residues (193–202, Figure 1B), initially thought to link the N-terminal domain and the C-terminal globular domain, appear to extend the long α-helix (Figure S12A,B). The superposition of the five best AlphaFold models of the full-length *B. subtilis* RNase Y monomer reveals a high mobility of the N-terminal and C-terminal domains relative to each other, with a hinge around residues 149-152 belonging to the turn (Figure 6A). This flexibility suggests that the turn in the coiled-coil structure is functionally relevant.

The fold of the globular C-terminal domain (residues 211–520), which includes the catalytic domain and a C-terminal region with unknown function (Figure 1B), consists of numerous α-helices and a few β-sheets (Figure S12A). The RNA binding module KH (residues 211–276), composed of three short α-helices and a three-strands β-sheet, is linked to the HD module (residues 336–429), composed of five α-helices, by two helices (residues 281–328). These three structural elements pack together to form the globular catalytic domain (residues 211–429), which is linked to the C-terminal region of unknown function (residues 438–520), composed of two α-helixes and a three-strands β-sheet, via a flexible linker.

The model of the full-length *B. subtilis* RNase Y dimer (Figure 6B–D) shows that dimerization involves both the N-terminal coiled-coil and the C-terminal domain. The supercoiling of the long N-terminal α-helices is well conserved between the models of the dimers of Nter-BsRNaseY and the full-length protein. Interestingly, the ten last C-terminal residues of the C-terminal region with unknown function are disordered in the monomer (Figure S12C) but completely structured, extending the last β-strand, in the dimer (Figure S12D). This structuration allows the C-terminal region to participate to the dimer interface, through packing interactions between the long last β-strand from each monomer (residues 505–519) (Figures S12E and S13A,C).

In most models of the full-length *B. subtilis* RNase Y (rank 1 to 4 for the monomer and rank 1 to 3 for the dimer), the globular C-terminal domain acts as an extension of the last helix (residues 152–192) observed in the model of Nter-BsRNaseY (Figure 6). Yet, in the less likely structures (rank 5 for the monomer and ranks 4 and 5 for the dimer), the globular domain folds up on the long N-terminal coiled-coil (Figure 6A,B). It remains to be seen whether this fold, made possible by the flexibility of the N- and C-terminal domains relative to each other, is physiologically relevant or not.

The predictions of AlphaFold for the full-length RNase Y in its monomeric/dimeric forms are still of good quality, although slightly lower than those for Nter-BsRNaseY (Figure S11C–E). Indeed, average pLDDT values were found to be 90.5/81.1 for the coiled-coil domain (residues 22–149) and 90.6/87.1 for the catalytic domain (residues 211–429), while residues with pLDDT values between 70 and 90 are expected to be modeled with an overall good backbone prediction [43]. Within the catalytic domain, the pLDDT values were 85.9/81.6 for the KH domain, 93.0/91.0 for the α-helices between the KH and HD domains, and 93.5/90.2 for the HD domain. The lowest pLDDT values were 84.7/77.4 for the C-terminal region of unknown function and 83.5/83.8 for residues 152–202 that correspond to the C-terminal extremity of the Nter-BsRNaseY construct, formed by one straight and one curved helix. Yet, the pLDDT value for this region was over 80 for the best model of the dimer, indicating that the predicted fold is still very likely. The loops connecting secondary structure elements (indicated by stars in Figure S11C–E) had lower pLDDT values than average, as expected.

## 4. Discussion

Here we studied the N-terminal domain of *B. subtilis* RNase Y using NMR to investigate its dimerization mode. Indeed, at the concentration used for the NMR studies (50–980 μM), Nter-BsRNaseY was in the dimeric form [32].

### *4.1. Interpretation of the NMR Data of Nter-BsRNaseY Using AlphaFold*

The 3D structures of the Nter-BsRNaseY monomer and dimer were modeled with AlphaFold and analyzed in light of the NMR data (Figures S14 and S15A). The NMR data showed that Nter-BsRNaseY is mainly in the helical form (65% at 300K) and that the helices ratio increased with decreasing temperature, as shown by the 1D spectra recorded from 318K to 288K (Figures 3B and S6). The AlphaFold model of the Nter-BsRNaseY dimer exhibited a long N-terminal parallel coiled-coil, followed by a turn, predicted to involve residues 149–151, and C-terminal helical ends that take part in dimer formation and can adopt two main conformations (Figure 5). Accordingly, it had previously been shown

by analyzing the binary interactions of the isolated domains of *B. subtilis* RNase Y that the N-terminal domain was a major contributor to the oligomerization of RNase Y [12]. The AlphaFold models appear to be more representative of what would happen at lower temperatures than those used to record the NMR spectra because these models contain more helices (97%, with 78% of the residues having pLDDT values over 90 for the best AlphaFold model).

The Nter-BsRNaseY dimer was found to form a parallel, and not an antiparallel coiled-coil helix, in agreement with the nice fit of the parallel model to the SEC-SAXS experimental data [32]. This fold, which is favored by hydrophobic and electrostatic interactions, as shown by the helical wheel diagrams (Figure S9), allows the anchoring of the N-terminal end of Nter-BsRNaseY to the cytoplasmic membrane via a transmembrane region (Figure 1B). Accordingly, all models generated with AlphaFold for the full-length RNase Y dimer also involved long parallel coiled-coils involving residues 1–149 (Figure 6B).

The α-helices predicted by TALOS to be the most temperature stable (residues 39–61, 73–88, and 122–149) correspond to a helical fold in the AlphaFold models (Figure S14). The most hydrophobic residues of these helices are involved in the dimerization surface in the best AlphaFold model (Figure S15B–D). Moreover, the TALOS-N predictions from our NMR data show a decrease in the propensity of residues 62–72 to be structured into a continuous helix (Figures 3A, S14 and S15A) that agrees with the break in the supercoil present in the AlphaFold models around this position. The helices predicted from the NMR data have the same boundaries as those in the AlphaFold models, except for residues 89–121 (Figures S14 and S15A). Indeed, this region is fully part of the helical dimeric interface generated by AlphaFold, whereas it is more flexible experimentally according to the NMR data obtained at 300K. This difference could be explained by the low ratio of hydrophobic residues in this region—i.e., present only at the position "d" of the heptad repeats (Figure S9B)—and by the high number of electrostatic interactions stabilizing this segment in the AlphaFold model (Figure S10D). The electrostatic interactions are probably reduced in the NMR experiment due to the addition of 200 mM NaCl in the samples, thus explaining the observed flexibility.

According to the backbone chemical shifts and $^{15}$N relaxation experiments (Figures 3 and 4), the N-terminal extremity of Nter-BsRNaseY was shown to be quite flexible. This flexibility agrees with the low pLDDT values for this region in the AlphaFold models (Figure 5D–F).

The $^{15}$N relaxation studies also indicated that the C-terminal extremity of Nter-BsRNaseY (residues 158–170) is rather flexible. This flexibility agrees with the AlphaFold models, in which it formed a dimer, with each monomer being constituted of either a bent or straight helix (Figure S15E). Moreover, splitting of the $^{1}$H-$^{15}$N HSQC signals was observed for several peaks belonging to the very C-terminal end (residues 171–191) (Figures 2C and S7), which is rich in both positively and negatively charged residues and also contains a stretch of hydrophobic residues (Figure S1). This splitting may result from a slow exchange on the NMR chemical shift time scale between at least two different conformations involving these last 20 residues, as proposed in the AlphaFold model (Figure S15E), where residues 158–192 of the two interacting chains have a different environment. The duplicated peaks disappeared upon an increase in temperature or a decrease in protein concentration, suggesting that dissociation of the dimer occurs at the very C-terminal end of Nter-BsRNaseY.

The relevance of the AlphaFold models was consolidated by our analysis of the HSQC-NOESY 3D spectra (Figure S5), since we were able to assign many intense $HN_i$-$HN_{i+1}$ and several low $HN_i$-$HN_{i+2}$ cross-peaks. Thus, altogether, the NMR data nicely support the α-helical fold of Nter-BsRNaseY proposed by AlphaFold, as well as its dimerization mode, not only at the N-terminal but also at the C-terminal end.

Finally, the best AlphaFold prediction for Nter-BsRNaseY was analyzed with DALI [58] to find the closest protein structures in the PDB, with a strong match being defined by a Z-score > (n/10) − 4, with n the number of residues. The highest structural homology

was found for the coiled-coil domain of SAS-6, a centriole protein (PDB code 6YRN, 11% sequence identity, Z score = 7.9, root mean square deviation (rmsd) of 3.9 Å for 111 aligned Cαs) [59]. SAS-6 fragments were shown to be organized as two-stranded parallel coiled-coil domains that could form higher-order interactions: nine SAS-6 dimers associated via interactions between their N-terminal globular head domain to form a ring. In addition, asymmetric parallel association between coiled-coil domains of SAS-6 was found to be important to form a cartwheel structure and provide polarity to the assembly.

### *4.2. AlphaFold Model of the Full-Length B. subtilis RNase Y*

To complement our NMR study, which was performed using a truncated *B. subtilis* RNase Y protein that lacks the C-terminal globular domain (residues 193–520), AlphaFold was used to generate a model of the full-length *B. subtilis* RNase Y, which was shown to exist as a dimer and possibly also as higher oligomeric forms [12]. Interestingly, in the model of the full-length protein, the coiled-coil structure observed for the Nter-BsRNAseY construct was extended by ten residues (Figure S12A,B) that were previously thought to belong to the C-terminal domain. Analysis of the assemblies with the Proteins Interfaces Structures and Assemblies (PISA) program [60] indicates that the coiled-coil structure contributes to ~72% of the buried surface area in the full-length dimer. Moreover, the models unveiled the probable fold of the C-terminal domain, which was unknown until this point. Intriguingly, the pLDDT values, especially for region 130–190, were lower for the full-length RNAse Y (Figure S11C–E) than for Nter-RNAseY (Figure 5D–F). This suggests an effect of the C-terminal domain on the conformation of residues 130–190.

The analysis of the best AlphaFold model of the C-terminal domain of *B. subtilis* RNase Y with DALI [58] revealed high structural similarity with proteins of known structure containing the HD or KH domains (Figure 1). Indeed, the highest structural homology was found for a protein predicted to belong to the HD hydrolase superfamily (PDB code 2PQ7, 24% sequence identity, unpublished), with a Z-score of 12.3 and an rmsd of 3.4 Å for 139 aligned Cαs. Interestingly, the latter protein was crystallized in the presence of divalent Fe atoms and superposition of the HD domains of both proteins highlights the potential binding mode of divalent metal ions to *B. subtilis* RNase Y, involving conserved His/Asp residues of the HD domain (Figure S16). Indeed, it is known that cleavage by RNase Y requires the presence of $Mg^{2+}$ ions, which can be replaced by $Mn^{2+}$ or $Zn^{2+}$ [6]. In addition, the C-terminal domain of *B. subtilis* RNase Y showed a high structural homology with the putative RNA-binding protein of the exosome complex (PDB code 2Z0S, 21% sequence identity, unpublished), with a Z-score of 12.2 and an rmsd of 1.8 Å for 81 aligned Cαs, and with the KH-containing RNA-binding protein RRP4 of the archaeal exosome (PDB code 2BA0, 21% sequence identity), with a Z-score of 11.8 and an rmsd of 1.7 Å for 78 aligned Cαs [61]. The exosome is a large multi-subunit RNase complex that is required for 3′/5′ processing of ribosomal RNA in archaea and eukaryotes and thus it has a similar function to RNase Y. The exosome structure consists of six RNase phosphorolytic (PH) domain subunits forming a hexameric ring, which associates with three KH and/or S1-containing subunits to form a regulatory RNA recognition platform that restricts entry to the catalytic chamber to unstructured RNA substrates.

The analysis of the C-terminal region with DALI identified several cation-binding proteins as close homologs, such as the cation efflux protein MamM (PDB code 3W64, 14% sequence identity, Z-score of 9.3, rmsd = 2.0 Å for 73 aligned Cαs) [62] and the cytoplasmic C-terminal domain of zinc transporter protein YiiP (PDB code 3H90, 11% sequence identity, Z-score of 7.8, rmsd = 2.3 Å for 72 aligned Cαs) [63]. MamM is one of the main ion transporters of magnetosomes, i.e., bacterial organelles that enable magnetotactic bacteria to orientate along geomagnetic fields. It was shown that the cytosolic domain of MamM forms a stable 'V-shape' dimer that undergoes distinct conformational changes upon divalent cation binding ([62], whereas the C-terminal domain of YiiP adopts a metallochaperone-like fold that allows it to deliver zinc ions to protein targets.

Finally, the C-terminal region of *B. subtilis* RNase Y was found to be homologous with proteins that are components of megadalton-sized ring-shaped complexes, such as protein PRGK (PDB code 2Y9J, 16% sequence identity, Z-score of 7.2, rmsd = 2.0 Å for 69 aligned Cαs) [64], or the flagellar M-ring protein FliF (PDB code 6SD3, 9% sequence identity, Z-score of 6.9, rmsd = 2.5 Å for 70 aligned Cαs) [65]. The homology of the C-terminal region of RNase Y with the abovementioned proteins should prompt investigation of whether it could be involved in the formation of a high-molecular weight oligomer. Finally, the structural analysis showed that the C-terminal domain of RNase Y is not structurally related to the N-terminal catalytic domain of RNase E.

The AlphaFold models of the full-length dimer of *B. subtilis* RNase Y also revealed a potential function of the C-terminal region as a dimerization domain. This is supported by the analysis of the assemblies with the PISA program [60], which indicated that, in solution, the C-terminal region should contribute to ~10% to the buried surface area in the full-length dimer. The dimerization function of the C-terminal region was not expected since previous bacterial two hybrid systems experiments did not reveal self-interactions of this region [12]. Furthermore, the dimeric interaction that involves the C-terminal regions of two monomers generates a hole in the structure of the dimer close to the KH domain (Figure S13A,B), suggesting that this hole, with a diameter of 12–13 Å, could be used to bind RNA. In this way, the KH domain could play a role in restricting access to the central chamber to unstructured RNA substrates, in a similar way to the RNA-binding module of the exosome complex [61]. This hypothesis agrees with the global electrostatic charge distribution of the dimeric C-terminal domain of *B. subtilis* RNase Y (Figure S13B,D), in which the KH domains, the last C-terminal β-sheets, and the residues forming the hole are positively charged and prone to bind a negatively charged molecule, such as RNA.

### *4.3. Interaction with Cellular Partners of the Degradosome Complex*

*B. subtilis* RNase Y fulfills a similar function to *E. coli* RNase E, which itself participates in a degradosome complex (Figure 1). In *E. coli*, RNase E forms the core of the degradosome, which in its minimal version includes polynucleotide phosphorylase (PNPase), the ATP-dependent DEAD-box RhlB RNA helicase (RhlB), and enolase [66] (Figure 1A). Several studies have suggested that the carboxy-terminal domain of RNase E acts as a flexible tether of the degradosome components. Our study shows that the C-terminal domain of *B. subtilis* RNase Y is not structurally related to the N-terminal catalytic domain of RNase E (Figure 1) [28]. Nevertheless, intriguingly, it has been previously shown that *E. coli* RNase E can effectively replace RNase Y in *B. subtilis* [28], and that the presence of the RNase E degradosome scaffold was not crucially important for the capacity of RNase E to complement for RNase Y.

However, similarly to *E. coli* RNase E, the N-terminal domain of *B. subtilis* RNase Y is flexible relative to the C-terminal globular domain, due to a turn involving residues 150–151, suggesting that the N-terminal domain could act as a tether to assemble the other degradosome proteins. In particular, several regions of the N-terminal region, such as peptide 62–72, which delineates a break in the supercoil, and peptide 89–121, which was shown to be the most flexible part in the coiled-coil, are likely candidates for binding degradosome proteins. Indeed, such interaction of a flexible protein region with several cellular partners (RNA or proteins) has previously been reported for other RNA-binding proteins [67–69].

Further insights into the function of the N-terminal domain of *B. subtilis* RNase Y will be obtained by studying its molecular interactions with its protein partners of the degradosome complex [28].

## 5. Conclusions

A coiled-coil is a structural element that is remarkable with respect to the diversity of conformations that it can adopt and for the range of functions that it exhibits [56]. As a result, long coiled-coil proteins encode an enormous repertoire of surface epitopes,

in addition to potentially linking functional domains or communicating conformational changes [70]. There are several examples of proteins that have coiled-coils that act as a scaffold for interaction with other proteins or other domains. For example, the flexibility of the coiled-coil was shown to regulate the function of soluble guanylate cyclase [71,72].

Elongated structures, such as coiled-coils that are under-represented in the PDB or structures that have never been observed previously, are difficult to predict using AlphaFold. Indeed, it was previously reported that, in the CENP-E kinesin AlphaFold model, the structure of the motor domain was well predicted, whereas the flexible coiled-coil appeared folded like a ball, not representing a biologically and functionally relevant state [73]. In this example, the AlphaFold prediction, based on the monomer, did not resolve the coiled-coil structure, the fold of which depended on dimerization. Similarly, it was reported that the single chain-based predictions of coiled-coils-containing centriolar or centrosomal proteins, as well as the models of heterodimeric or multimeric coiled-coil assemblies, lacked structural plausibility [74]. Yet, AlphaFold has been shown to be successful in predicting long coiled-coils in several cases, such as human alpha or beta soluble guanylate cyclase [72].

Our multidimensional heteronuclear NMR study of Nter-BsRNaseY showed that this domain adopts a helix-type secondary structure over almost the entire sequence, in full agreement with the model calculated by AlphaFold. In our case, AlphaFold was also successful in predicting two conformations for the C-terminal helix, which were confirmed by our relaxation experiments. Although transient interactions are not expected to be captured by AlphaFold and the prediction of multimers is still at its beginning [75], here, we showed a case where AlphaFold was particularly useful to produce a reliable 3D model that helped to interpret the NMR data.

**Supplementary Materials:** The following supporting information can be downloaded at: https://www.mdpi.com/article/10.3390/biom12121798/s1, Figure S1: Secondary structure prediction of Nter-BsRNaseY; Figure S2: Characterization of Nter-BsRNaseY by SEC and CD; Figure S3: ($^{1}$H-$^{15}$N)-HMQC spectra of Nter-BsRNaseY in the absence and presence of urea; Figure S4: Representative strips from the 3D HNCA and HN(CO)CA spectra; Figure S5: $^{1}$H-$^{15}$N NOESY-HSQC strips showing several examples of NOE peak assignments; Figure S6: Temperature effect on the amide and aromatic and aliphatic protons of Nter-BsRNAseY; Figure S7: Dependence on the temperature of the duplicated cross-peaks in the $^{1}$H-$^{15}$N BEST-TROSY spectra; Figure S8: Effect of Nter-BsRNaseY concentration on the $^{1}$H-$^{15}$N BEST-TROSY NMR spectra; Figure S9: Helical wheel representation of the helices predicted in the best AlphaFold model of the Nter-BsRNaseY dimer; Figure S10: Hydrophobic and electrostatic interactions in the best structure of the Nter-BsRNAseY dimer generated by AlphaFold; Figure S11: 3D models of the full-length *B. subtilis* RNase Y predicted by AlphaFold; Figure S12. Best AlphaFold models for the C-terminal domain in the *B. subtilis* RNase Y monomer and dimer; Figure S13: Dimeric interface of the C-terminal domain of the best AlphaFold model for the full-length *B. subtilis* RNase Y; Figure S14: Comparison of the α-helices propensity of the Nter-BsRNaseY dimer, determined experimentally from the NMR chemical shifts or calculated with AlphaFold; Figure S15: Comparison of the α-helices propensity determined experimentally from the backbone NMR chemical shifts at 300K using TALOS and the AlphaFold Nter-BsRNaseY best dimer 3D model; Figure S16: Potential binding mode of divalent ions to the HD domain of *B. subtilis* RNase Y. Table S1: Prediction of α-helices propensity using the α-helix prediction calculated by TALOS-N.

**Author Contributions:** Conceptualization, N.M., C.v.H. and B.G.-P.; methodology, N.M. and C.v.H.; software, N.M.; formal analysis, N.M., C.v.H. and B.G.-P.; investigation, P.H., N.A., N.M. and B.G.-P.; data curation, N.M. and C.v.H.; writing—original draft preparation, N.M. and B.G.-P.; writing—review and editing, N.M., C.v.H. and B.G.-P.; visualization, N.M.; supervision, C.v.H. and B.G.-P.; funding acquisition, C.v.H. and B.G.-P. All authors have read and agreed to the published version of the manuscript.

**Funding:** This work was supported by the French State Program 'Investissements d'Avenir' (Grants "LABEX DYNAMO", ANR-11-LABX-0011 and ANR-11-BSV8-026). Financial support from the IR INFRANALYTICS FR2054 for conducting the research is also gratefully acknowledged.

**Data Availability Statement:** Resonance assignments for Nter-BsRNAseY at 303K were deposited in BMRB accession number 51229.

**Acknowledgments:** We thank Djemel Hamdane for performing the CD data collection and analysis, Christophe Velours for performing the SEC-MALS experiments, the Macromolecular Interaction Platform of I2BC for use of its facilities, Charles Bou-Nader for initiating the NMR project and for fruitful initial discussions, Ludovic Pecqueur for preliminary experiments and fruitful discussions, and Harald Putzer for discussions relative to RNase Y.

**Conflicts of Interest:** The authors declare no conflict of interest.

## References

1. Laalami, S.; Putzer, H. mRNA degradation and maturation in prokaryotes: The global players. *Biomol. Concepts* **2011**, *2*, 491–506. [CrossRef] [PubMed]
2. Laalami, S.; Zig, L.; Putzer, H. Initiation of mRNA decay in bacteria. *Cell Mol. Life Sci.* **2014**, *71*, 1799–1828. [CrossRef] [PubMed]
3. Mohanty, B.K.; Kushner, S.R. Regulation of mRNA Decay in Bacteria. *Annu. Rev. Microbiol.* **2016**, *70*, 25–44. [CrossRef] [PubMed]
4. Gorna, M.W.; Carpousis, A.J.; Luisi, B.F. From conformational chaos to robust regulation: The structure and function of the multi-enzyme RNA degradosome. *Q. Rev. Biophys.* **2012**, *45*, 105–145. [CrossRef] [PubMed]
5. Mackie, G.A. RNase E: At the interface of bacterial RNA processing and decay. *Nat. Rev. Microbiol.* **2013**, *11*, 45–57. [CrossRef] [PubMed]
6. Shahbabian, K.; Jamalli, A.; Zig, L.; Putzer, H. RNase Y, a novel endoribonuclease, initiates riboswitch turnover in *Bacillus subtilis*. *EMBO J.* **2009**, *28*, 3523–3533. [CrossRef]
7. Durand, S.; Tomasini, A.; Braun, F.; Condon, C.; Romby, P. sRNA and mRNA turnover in Gram-positive bacteria. *FEMS Microbiol. Rev.* **2015**, *39*, 316–330. [CrossRef]
8. Kaito, C.; Kurokawa, K.; Matsumoto, Y.; Terao, Y.; Kawabata, S.; Hamada, S.; Sekimizu, K. Silkworm pathogenic bacteria infection model for identification of novel virulence genes. *Mol. Microbiol.* **2005**, *56*, 934–944. [CrossRef]
9. Bonnin, R.A.; Bouloc, P. RNA Degradation in *Staphylococcus aureus*: Diversity of Ribonucleases and Their Impact. *Int. J. Genom.* **2015**, *2015*, 395753. [CrossRef]
10. Obana, N.; Nakamura, K.; Nomura, N. Role of RNase Y in *Clostridium perfringens* mRNA Decay and Processing. *J. Bacteriol.* **2017**, *199*. [CrossRef]
11. Kang, S.O.; Caparon, M.G.; Cho, K.H. Virulence gene regulation by CvfA, a putative RNase: The CvfA-enolase complex in *Streptococcus pyogenes* links nutritional stress, growth-phase control, and virulence gene expression. *Infect. Immun.* **2010**, *78*, 2754–2767. [CrossRef] [PubMed]
12. Lehnik-Habrink, M.; Newman, J.; Rothe, F.M.; Solovyova, A.S.; Rodrigues, C.; Herzberg, C.; Commichau, F.M.; Lewis, R.J.; Stulke, J. RNase Y in *Bacillus subtilis*: A Natively disordered protein that is the functional equivalent of RNase E from *Escherichia coli*. *J. Bacteriol.* **2011**, *193*, 5431–5441. [CrossRef] [PubMed]
13. Callaghan, A.J.; Grossmann, J.G.; Redko, Y.U.; Ilag, L.L.; Moncrieffe, M.C.; Symmons, M.F.; Robinson, C.V.; McDowall, K.J.; Luisi, B.F. Quaternary structure and catalytic activity of the *Escherichia coli* ribonuclease E amino-terminal catalytic domain. *Biochemistry* **2003**, *42*, 13848–13855. [CrossRef] [PubMed]
14. Callaghan, A.J.; Marcaida, M.J.; Stead, J.A.; McDowall, K.J.; Scott, W.G.; Luisi, B.F. Structure of *Escherichia coli* RNase E catalytic domain and implications for RNA turnover. *Nature* **2005**, *437*, 1187–1191. [CrossRef] [PubMed]
15. Koslover, D.J.; Callaghan, A.J.; Marcaida, M.J.; Garman, E.F.; Martick, M.; Scott, W.G.; Luisi, B.F. The crystal structure of the *Escherichia coli* RNase E apoprotein and a mechanism for RNA degradation. *Structure* **2008**, *16*, 1238–1244. [CrossRef]
16. Vanzo, N.F.; Li, Y.S.; Py, B.; Blum, E.; Higgins, C.F.; Raynal, L.C.; Krisch, H.M.; Carpousis, A.J. Ribonuclease E organizes the protein interactions in the *Escherichia coli* RNA degradosome. *Genes Dev.* **1998**, *12*, 2770–2781. [CrossRef]
17. Dominguez-Malfavon, L.; Islas, L.D.; Luisi, B.F.; Garcia-Villegas, R.; Garcia-Mena, J. The assembly and distribution in vivo of the *Escherichia coli RNA* degradosome. *Biochimie* **2013**, *95*, 2034–2041. [CrossRef]
18. Ait-Bara, S.; Carpousis, A.J.; Quentin, Y. RNase E in the gamma-Proteobacteria: Conservation of intrinsically disordered noncatalytic region and molecular evolution of microdomains. *Mol. Genet. Genom.* **2015**, *290*, 847–862. [CrossRef]
19. Bruce, H.A.; Du, D.; Matak-Vinkovic, D.; Bandyra, K.J.; Broadhurst, R.W.; Martin, E.; Sobott, F.; Shkumatov, A.V.; Luisi, B.F. Analysis of the natively unstructured RNA/protein-recognition core in the *Escherichia coli* RNA degradosome and its interactions with regulatory RNA/Hfq complexes. *Nucleic Acids Res.* **2018**, *46*, 387–402. [CrossRef]
20. Callaghan, A.J.; Aurikko, J.P.; Ilag, L.L.; Gunter Grossmann, J.; Chandran, V.; Kuhnel, K.; Poljak, L.; Carpousis, A.J.; Robinson, C.V.; Symmons, M.F.; et al. Studies of the RNA degradosome-organizing domain of the *Escherichia coli* ribonuclease RNase E. *J. Mol. Biol.* **2004**, *340*, 965–979. [CrossRef]
21. Marcaida, M.J.; DePristo, M.A.; Chandran, V.; Carpousis, A.J.; Luisi, B.F. The RNA degradosome: Life in the fast lane of adaptive molecular evolution. *Trends Biochem. Sci.* **2006**, *31*, 359–365. [CrossRef] [PubMed]
22. Khemici, V.; Poljak, L.; Luisi, B.F.; Carpousis, A.J. The RNase E of *Escherichia coli* is a membrane-binding protein. *Mol. Microbiol.* **2008**, *70*, 799–813. [CrossRef] [PubMed]

23. Nurmohamed, S.; McKay, A.R.; Robinson, C.V.; Luisi, B.F. Molecular recognition between *Escherichia coli* enolase and ribonuclease E. *Acta Crystallogr. D Biol. Crystallogr.* **2010**, *66*, 1036–1040. [CrossRef] [PubMed]
24. Chandran, V.; Luisi, B.F. Recognition of enolase in the *Escherichia coli* RNA degradosome. *J. Mol. Biol.* **2006**, *358*, 8–15. [CrossRef] [PubMed]
25. Nurmohamed, S.; Vaidialingam, B.; Callaghan, A.J.; Luisi, B.F. Crystal structure of *Escherichia coli* polynucleotide phosphorylase core bound to RNase E, RNA and manganese: Implications for catalytic mechanism and RNA degradosome assembly. *J. Mol. Biol.* **2009**, *389*, 17–33. [CrossRef] [PubMed]
26. Grishin, N.V. KH domain: One motif, two folds. *Nucleic Acids Res.* **2001**, *29*, 638–643. [CrossRef]
27. Aravind, L.; Koonin, E.V. The HD domain defines a new superfamily of metal-dependent phosphohydrolases. *Trends Biochem. Sci.* **1998**, *23*, 469–472. [CrossRef]
28. Laalami, S.; Cavaiuolo, M.; Roque, S.; Chagneau, C.; Putzer, H. *Escherichia coli* RNase E can efficiently replace RNase Y in *Bacillus subtilis*. *Nucleic Acids Res.* **2021**, *49*, 4643–4654. [CrossRef]
29. Lehnik-Habrink, M.; Schaffer, M.; Mader, U.; Diethmaier, C.; Herzberg, C.; Stulke, J. RNA processing in *Bacillus subtilis*: Identification of targets of the essential RNase Y. *Mol. Microbiol.* **2011**, *81*, 1459–1473. [CrossRef]
30. Karimova, G.; Pidoux, J.; Ullmann, A.; Ladant, D. A bacterial two-hybrid system based on a reconstituted signal transduction pathway. *Proc. Natl. Acad. Sci. USA* **1998**, *95*, 5752–5756. [CrossRef]
31. Lupas, A.; Van Dyke, M.; Stock, J. Predicting coiled coils from protein sequences. *Science* **1991**, *252*, 1162–1164. [CrossRef]
32. Hardouin, P.; Velours, C.; Bou-Nader, C.; Assrir, N.; Laalami, S.; Putzer, H.; Durand, D.; Golinelli-Pimpaneau, B. Dissociation of the Dimer of the Intrinsically Disordered Domain of RNase Y upon Antibody Binding. *Biophys. J.* **2018**, *115*, 2102–2113. [CrossRef] [PubMed]
33. Commichau, F.M.; Rothe, F.M.; Herzberg, C.; Wagner, E.; Hellwig, D.; Lehnik-Habrink, M.; Hammer, E.; Volker, U.; Stulke, J. Novel activities of glycolytic enzymes in *Bacillus subtilis*: Interactions with essential proteins involved in mRNA processing. *Mol. Cell Proteom.* **2009**, *8*, 1350–1360. [CrossRef] [PubMed]
34. Lehnik-Habrink, M.; Lewis, R.J.; Mader, U.; Stulke, J. RNA degradation in *Bacillus subtilis*: An interplay of essential endo- and exoribonucleases. *Mol. Microbiol.* **2012**, *84*, 1005–1017. [CrossRef] [PubMed]
35. Lehnik-Habrink, M.; Pfortner, H.; Rempeters, L.; Pietack, N.; Herzberg, C.; Stulke, J. The RNA degradosome in *Bacillus subtilis*: Identification of CshA as the major RNA helicase in the multiprotein complex. *Mol. Microbiol.* **2010**, *77*, 958–971. [CrossRef]
36. Newman, J.A.; Hewitt, L.; Rodrigues, C.; Solovyova, A.S.; Harwood, C.R.; Lewis, R.J. Dissection of the network of interactions that links RNA processing with glycolysis in the *Bacillus subtilis* degradosome. *J. Mol. Biol.* **2012**, *416*, 121–136. [CrossRef] [PubMed]
37. Salvo, E.; Alabi, S.; Liu, B.; Schlessinger, A.; Bechhofer, D.H. Interaction of *Bacillus subtilis* Polynucleotide Phosphorylase and RNase Y: Structural Mapping and effect on mRNA turnover. *J. Biol. Chem.* **2016**, *291*, 6655–6663. [CrossRef] [PubMed]
38. Cho, K.H. The Structure and Function of the Gram-Positive Bacterial RNA Degradosome. *Front. Microbiol.* **2017**, *8*, 154. [CrossRef]
39. Liu, H.; Jeffery, C.J. Moonlighting Proteins in the Fuzzy Logic of Cellular Metabolism. *Molecules* **2020**, *25*, 3440. [CrossRef]
40. Antikainen, J.; Kuparinen, V.; Lahteenmaki, K.; Korhonen, T.K. Enolases from Gram-positive bacterial pathogens and commensal lactobacilli share functional similarity in virulence-associated traits. *FEMS Immunol. Med. Microbiol.* **2007**, *51*, 526–534. [CrossRef]
41. Agarwal, S.; Kulshreshtha, P.; Bambah Mukku, D.; Bhatnagar, R. alphaa-Enolase binds to human plasminogen on the surface of *Bacillus anthracis*. *Biochim Biophys. Acta* **2008**, *1784*, 986–994. [CrossRef] [PubMed]
42. Esgleas, M.; Li, Y.; Hancock, M.A.; Harel, J.; Dubreuil, J.D.; Gottschalk, M. Isolation and characterization of alpha-enolase, a novel fibronectin-binding protein from *Streptococcus suis*. *Microbiology* **2008**, *154*, 2668–2679. [CrossRef] [PubMed]
43. Jumper, J.; Evans, R.; Pritzel, A.; Green, T.; Figurnov, M.; Ronneberger, O.; Tunyasuvunakool, K.; Bates, R.; Žídek, A.; Potapenko, A.; et al. Highly accurate protein structure prediction with AlphaFold. *Nature* **2021**, *596*, 583–589. [CrossRef]
44. Kelley, L.A.; Mezulis, S.; Yates, C.M.; Wass, M.N.; Sternberg, M.J. The Phyre2 web portal for protein modeling, prediction and analysis. *Nat. Protoc.* **2015**, *10*, 845–858. [CrossRef] [PubMed]
45. McGuffin, L.J.; Bryson, K.; Jones, D.T. The PSIPRED protein structure prediction server. *Bioinformatics* **2000**, *16*, 404–405. [CrossRef]
46. Combet, C.; Blanchet, C.; Geourjon, C.; Deléage, G. NPS@: Network protein sequence analysis. *Trends Biochem. Sci.* **2000**, *25*, 147–150. [CrossRef]
47. Grigoryan, G.; Keating, A.E. Structural specificity in coiled-coil interactions. *Curr. Opin. Struct. Biol.* **2008**, *18*, 477–483. [CrossRef]
48. Mirdita, M.; Schütze, K.; Moriwaki, Y.; Heo, L.; Ovchinnikov, S.; Steinegger, M. ColabFold—Making protein folding accessible to all. *bioRxiv* **2021**. [CrossRef]
49. DeLano, W.L. The PyMOL Molecular Graphics System. 2002. Available online: https://pymol.org/2/ (accessed on 22 September 2022).
50. Vranken, W.F.; Boucher, W.; Stevens, T.J.; Fogh, R.H.; Pajon, A.; Llinas, M.; Ulrich, E.L.; Markley, J.L.; Ionides, J.; Laue, E.D. The CCPN data model for NMR spectroscopy: Development of a software pipeline. *Proteins* **2005**, *59*, 687–696. [CrossRef]
51. Trainor, K.; Palumbo, J.A.; MacKenzie, D.W.S.; Meiering, E.M. Temperature dependence of NMR chemical shifts: Tracking and statistical analysis. *Protein Sci.* **2020**, *29*, 306–314. [CrossRef]
52. Das, A.; Mukhopadhyay, C. Urea-mediated protein denaturation: A consensus view. *J. Phys. Chem. B* **2009**, *113*, 12816–12824. [CrossRef] [PubMed]

53. Shen, Y.; Bax, A. Protein backbone and sidechain torsion angles predicted from NMR chemical shifts using artificial neural networks. *J. Biomol. NMR* **2013**, *56*, 227–241. [CrossRef]
54. Cierpicki, T.; Otlewski, J. Amide proton temperature coefficients as hydrogen bond indicators in proteins. *J. Biomol. NMR* **2001**, *21*, 249–261. [CrossRef]
55. Ishima, R. Recent developments in (15)N NMR relaxation studies that probe protein backbone dynamics. *Top Curr. Chem.* **2012**, *326*, 99–122. [CrossRef]
56. Mason, J.M.; Arndt, K.M. Coiled coil domains: Stability, specificity, and biological implications. *Chembiochem* **2004**, *5*, 170–176. [CrossRef] [PubMed]
57. Mondal, S.; Basavalingappa, V.; Jacoby, G.; Shimon, L.J.W.; Beck, R.; Gazit, E. Functional Coiled-Coil-like Assembly by Knob-into-Hole Packing of Single Heptad Repeat. *ACS Nano* **2019**, *13*, 12630–12637. [CrossRef]
58. Chao, J.A.; Prasad, G.S.; White, S.A.; Stout, C.D.; Williamson, J.R. Inherent protein structural flexibility at the RNA-binding interface of L30e. *J. Mol. Biol.* **2003**, *326*, 999–1004. [CrossRef] [PubMed]
59. Varadi, M.; Zsolyomi, F.; Guharoy, M.; Tompa, P. Functional Advantages of Conserved Intrinsic Disorder in RNA-Binding Proteins. *PLoS ONE* **2015**, *10*, e0139731. [CrossRef] [PubMed]
60. Baudin, A.; Moreno-Romero, A.K.; Xu, X.; Selig, E.E.; Penalva, L.O.F.; Libich, D.S. Structural Characterization of the RNA-Binding Protein SERBP1 Reveals Intrinsic Disorder and Atypical RNA Binding Modes. *Front. Mol. Biosci.* **2021**, *8*, 744707. [CrossRef]
61. Weichsel, A.; Kievenaar, J.A.; Curry, R.; Croft, J.T.; Montfort, W.R. Instability in a coiled-coil signaling helix is conserved for signal transduction in soluble guanylyl cyclase. *Protein Sci.* **2019**, *28*, 1830–1839. [CrossRef]
62. Horst, B.G.; Yokom, A.L.; Rosenberg, D.J.; Morris, K.L.; Hammel, M.; Hurley, J.H.; Marletta, M.A. Allosteric activation of the nitric oxide receptor soluble guanylate cyclase mapped by cryo-electron microscopy. *eLife* **2019**, *8*, e50634. [CrossRef]
63. Holm, L. Using Dali for Protein Structure Comparison. *Methods Mol. Biol.* **2020**, *2112*, 29–42. [CrossRef]
64. Kantsadi, A.L.; Hatzopoulos, G.N.; Gönczy, P.; Vakonakis, I. Structures of SAS-6 coiled coil hold implications for the polarity of the centriolar cartwheel. *Structure* **2022**, *30*, 671–684.e5. [CrossRef]
65. Krissinel, E.; Henrick, K. Inference of macromolecular assemblies from crystalline state. *J. Mol. Biol.* **2007**, *372*, 774–797. [CrossRef]
66. Büttner, K.; Wenig, K.; Hopfner, K.P. Structural framework for the mechanism of archaeal exosomes in RNA processing. *Mol. Cell* **2005**, *20*, 461–471. [CrossRef] [PubMed]
67. Zeytuni, N.; Uebe, R.; Maes, M.; Davidov, G.; Baram, M.; Raschdorf, O.; Nadav-Tsubery, M.; Kolusheva, S.; Bitton, R.; Goobes, G.; et al. Cation diffusion facilitators transport initiation and regulation is mediated by cation induced conformational changes of the cytoplasmic domain. *PLoS ONE* **2014**, *9*, e92141. [CrossRef] [PubMed]
68. Lu, M.; Chai, J.; Fu, D. Structural basis for autoregulation of the zinc transporter YiiP. *Nat. Struct. Mol. Biol.* **2009**, *16*, 1063–1067. [CrossRef]
69. Schraidt, O.; Marlovits, T.C. Three-dimensional model of *Salmonella*'s needle complex at subnanometer resolution. *Science* **2011**, *331*, 1192–1195. [CrossRef] [PubMed]
70. Johnson, S.; Fong, Y.H.; Deme, J.C.; Furlong, E.J.; Kuhlen, L.; Lea, S.M. Symmetry mismatch in the MS-ring of the bacterial flagellar rotor explains the structural coordination of secretion and rotation. *Nat. Microbiol.* **2020**, *5*, 966–975. [CrossRef] [PubMed]
71. Carpousis, A.J. The RNA degradosome of *Escherichia coli*: An mRNA-degrading machine assembled on RNase E. *Annu. Rev. Microbiol.* **2007**, *61*, 71–87. [CrossRef]
72. Truebestein, L.; Leonard, T.A. Coiled-coils: The long and short of it. *Bioessays* **2016**, *38*, 903–916. [CrossRef] [PubMed]
73. Perrakis, A.; Sixma, T.K. AI revolutions in biology: The joys and perils of AlphaFold. *EMBO Rep.* **2021**, *22*, e54046. [CrossRef] [PubMed]
74. Van Breugel, M.; Rosa, E.; Silva, I.; Andreeva, A. Structural validation and assessment of AlphaFold2 predictions for centrosomal and centriolar proteins and their complexes. *Commun. Biol.* **2022**, *5*, 312. [CrossRef] [PubMed]
75. Evans, R.; O'Neill, M.; Pritzel, A.; Antropova, N.; Senior, A.; Green, T.; Žídek, A.; Bates, R.; Blackwell, S.; Yim, J.; et al. Protein complex prediction with AlphaFold-Multimer. *bioRxiv* **2021**, 10.04.463034.